INTERNATIONAL JOURNAL FOR NUMERICAL METHODS IN FLUIDS, VOL. 23, 711–732 (1996)

NUMERICAL STUDY OF HIGH-REYNOLDS-NUMBER FLOW PAST A BLUFF OBJECT

MO-HONG CHOU AND WEICHENG HUANG

Institute of Mathematics, Academia Sinica, Nankang, Taipei 11529, Taiwan

SUMMARY

A semi-explicit finite difference scheme is proposed to study unsteady two-dimensional, incompressible flow past a bluff object at high Reynolds number. The bluff object comes from a class of elliptical cylinders in which the aspect ratio and the angle of attack are two controlled parameters. Associated with the streamfunction–vorticity formulation, the interior vorticity, streamfunction and wall vorticity are updated in turn for each time step. The streamfunction and wall vorticity are solved by means of a multigrid method and a projection method respectively. In regard to the vorticity transport equation, implicitness is merely associated with the diffusion operator, which can be made semi-explicit via approximate factorization. Low-diffusive upwinding is devised to handle the convection part. Numerical results are reported for Reynolds numbers up to 40,000. Comparisons with other numerical or physical experiments are included.

KEY WORDS: finite difference scheme; prowake co-ordinates; vorticity conditioning; high-order upwinding; semi-explicit time marching; bluff object

1. INTRODUCTION

The numerical simulation of unsteady two-dimensional, incompressible flow past a bluff object at high Reynolds number has been a challenge to computational fluid dynamicists for years. Theoretically the bluff object is often modelled as an elliptical cylinder in which the aspect ratio and the angle of attack are two controlled parameters. Of this class, flow past a circular cylinder is the most oft-cited case. Although the geometry is simple, the flow pattern in the proximity of the circular cylinder is full of variety. See for example the works of Bouard and Coutanceau[1] and Loc and Bouard[2] for the early-stage development and Kawamura and Kuwahara[3] for the fully developed case.

As far as numerical simulation is concerned, almost all popular methods such as finite difference, finite element, spectral and vortex particles have already been employed and improved in certain ways in past years. However, we shall concentrate our attention on the development of finite difference schemes. Even within this category one can find that the methodology is also full of variety owing to the coexistent advantage and drawback in each individual method. As a consequence one can see from the literature some data discrepancy among the common points of interest such as the development of the primary unsteady wake, the formation of secondary vortices, the evolution of drag and lift coefficients as well as the history of the separation angle. Brief surveys of previous works can be found for example in References 2–8.

CCC 0271–2091/96/070711–22

Received November 1995
Revised January 1996

The progress in numerical algorithms is of course accompanied by the remarkable advance in computer power. The combined efforts have moved the effective Reynolds number up several orders in magnitude during past decades. As more and more complex phenomena are revealed, it certainly continues to be an active research area.

Finite difference schemes are preferred here because they feature in ease of algorithm design and programming, especially when one wants to take advantage of modern computing facilities such as vectorisation and parallelism. Prior to using this feature, we have to solve certain basic issues on the algorithmic side, however. Similar issues also appear in any other preferred method.

In conjunction with the streamfunction–vorticity formulation of the Navier–Stokes equations we are concerned for example with the grid generation, upwinding technique, wall vorticity condition and stable time-marching procedure, which has minor impact on speed-up considerations such as multigrid and vectorization. These topics have certainly been addressed by many authors but without a unified approach.

In this work we shall make a contribution to these points and propose a semi-explicit scheme which improves some ideas used in our previous works.[9,10] By semi-explicit we mean that the set of linear equations related to the semi-implicit treatment of the vorticity transport equation can be solved directly via a time-independent approximate factorization. Both early-stage and long-term simulations are performed for flow past an elliptical cylinder with various combinations of aspect ratio and angle of attack at Reynolds numbers up to 4×10^4. Comparisons with other numerical or physical experiments are included.

2. PROBLEM FORMULATION

In this work we shall consider a uniform incompressible flow, with velocity $(U_\infty, 0)$ at infinity, past a bluff object whose boundary in the xy-plane is characterized by

$$x + \mathrm{i}y = \tfrac{1}{2}[(1+\lambda)z + (1-\lambda)\mathrm{e}^{-2\mathrm{i}\Theta}/z], \quad \text{where } \mathrm{i} \equiv \sqrt{(-1)} \text{ and } |z| \equiv 1. \tag{1}$$

According to (1), the geometry is an ellipse with the parameter λ indicating the aspect ratio of the short axis over the long axis (hence $0 \leqslant \lambda \leqslant 1$). The other parameter Θ indicates the angle of attack to the incoming flow (see Figure 1 for a sketch). In what follows, Θ will be mentioned in degrees with a tacit conversion to radians. Setting $(\lambda, \Theta) = (1, 90°)$, for example, yields flow past a circular cylinder.

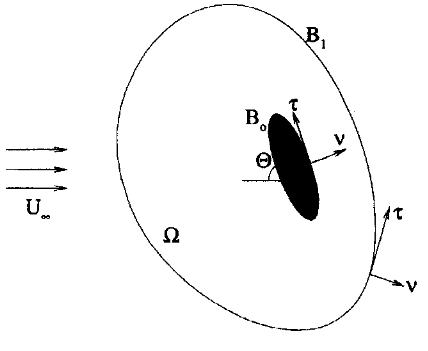

Figure 1. Illustration of Theorem 1 for wall vorticity conditioning

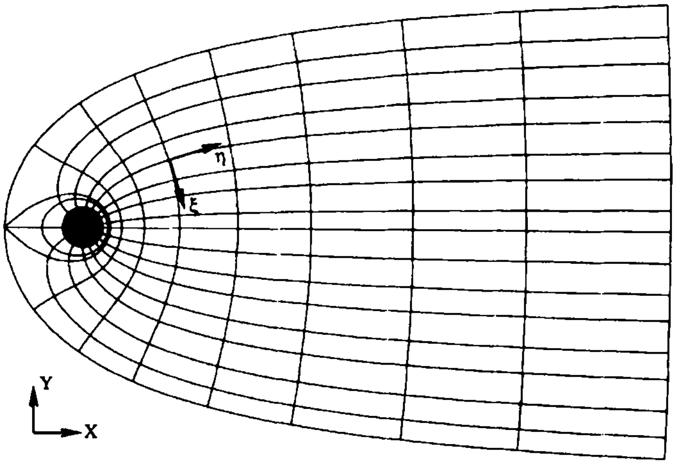

Figure 2. Sketch of prowake, orthogonal grid system

The flow is governed by the Navier–Stokes equations, which after non-dimensionalization are written in terms of vorticity (ω) and streamfunction (ψ) as

$$\omega_t + \psi_y \omega_x - \psi_x \omega_y = \frac{2}{R}(\omega_{xx} + \omega_{yy}), \tag{2}$$

$$\psi_{xx} + \psi_{yy} = -\omega, \tag{3}$$

$$\psi = \psi_x = \psi_y = 0 \quad \text{on object's boundary for } t > 0, \tag{4}$$

$$(\psi_x, \psi_y) \rightarrow (0, 1) \quad \text{as } x^2 + y^2 \rightarrow \infty, \tag{5}$$

$$\psi(x, y, t = 0) = \psi^{\circ}(x, y) \equiv \text{potential flow}. \tag{6}$$

In equations (1)–(6) the underlying length scale is $D/2$, where D denotes the largest distance between any two points located on the object's boundary (e.g. $D =$ diameter of a circle or long axis of an ellipse), while the Reynolds number R is defined as $R = DU_{\infty}/\nu$, where ν stands for the kinematic viscosity.

It has been shown that a generally feasible approach to solve equations (2)–(6) is direct numerical simulation. Finite difference schemes are adopted here. To facilitate the associated computations, a body-fitted orthogonal co-ordinate system is desired, which is constructed through a sequence of transformations as stated below.

The sequence was started with equation (1), by which the fluid region in the z-plane becomes exterior to a unit circle. For high-Reynolds-number flow problems, (1) is followed by the 'prowake' transformation $z = z(\zeta)$ (see Figure 2 for a sketch), in which

$$\zeta = \xi + \mathrm{i}\tilde{\eta} = \frac{\mathrm{i}}{2}(z - 1/z) + \frac{\mathrm{i}\Gamma}{\pi}\log(z) \quad \text{for } -\Gamma \leqslant \xi \leqslant \Gamma \text{ and } \tilde{\eta} \geqslant 0. \tag{7}$$

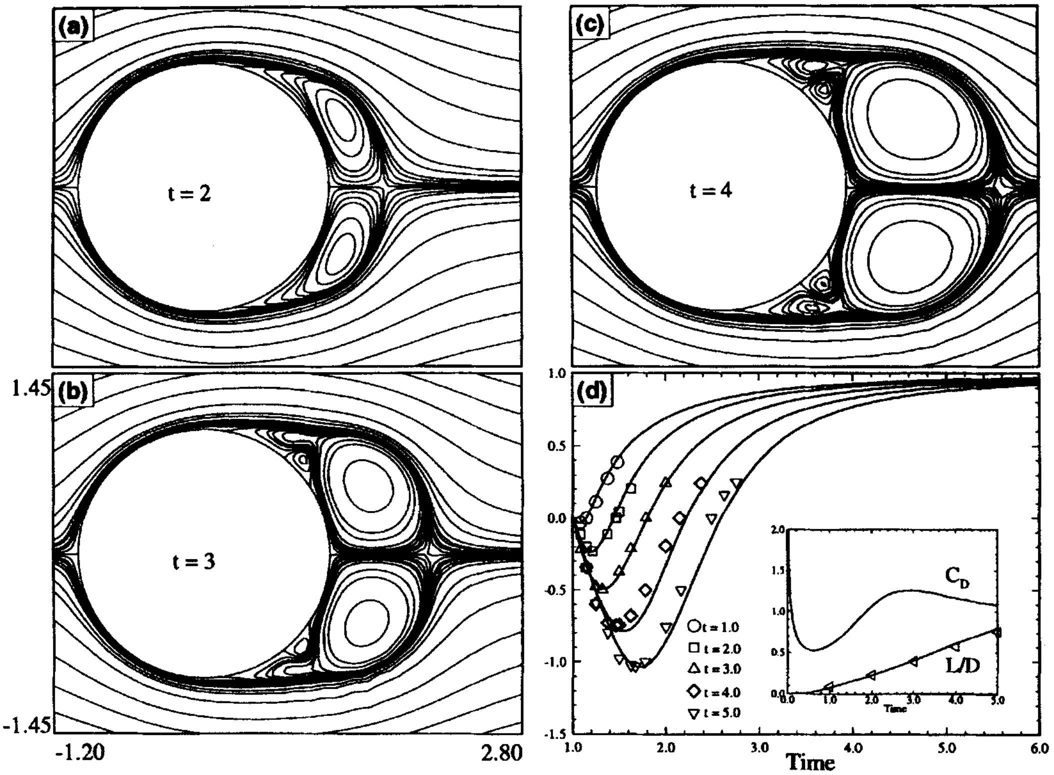

Figure 3. Early evolution of flow past an impulsively started circular cylinder at $R = 1000$. (a)–(c) Streamline plots at $t = 2, 3, 4$. (d) Radial velocity along symmetry axis behind cylinder at $t = 1, 2, 3, 4, 5$. Shown in the inset are the drag coefficient (C_D) and wake length (L/D). ————, present; symbols, Reference 6

To achieve the desired resolution ($= \mathcal{O}(1/\sqrt{R})$) in the proximity of the object economically, a quadratic scaling in the $\tilde{\eta}$-direction is introduced:

$$\tilde{\eta} = \eta(a + b\eta) \equiv f(\eta), \quad \eta \geqslant 0, \quad \text{where } a \text{ and } b \text{ are positive constants.} \tag{8}$$

By virtue of (1), (7) and (8) the Navier–Stokes equations (2) and (3) are transformed into the following version. For $(\xi, \eta) \in [-\Gamma, \Gamma] \times [0, \eta_\infty]$,

$$(Jf'^2)\omega_t + f'(\psi_\eta \omega_\xi - \psi_\xi \omega_\eta) = \frac{2}{R}\left(f'^2 \omega_{\xi\xi} - \frac{f''}{f'}\omega_\eta + \omega_{\eta\eta}\right), \tag{9}$$

$$f'^2 \psi_{\xi\xi} - \frac{f''}{f'}\psi_\eta + \psi_{\eta\eta} = -(Jf'^2)\omega. \tag{10}$$

In (9) and (10), $J = \partial(x, y)/\partial(\xi, \tilde{\eta})$ is the Jacobian of the conformal mapping composed of (1) and (7), while f' and f'' denote the first and second derivatives of f defined in (8) respectively. Note that in the sequel J is modified to denote the combined term Jf'^2.

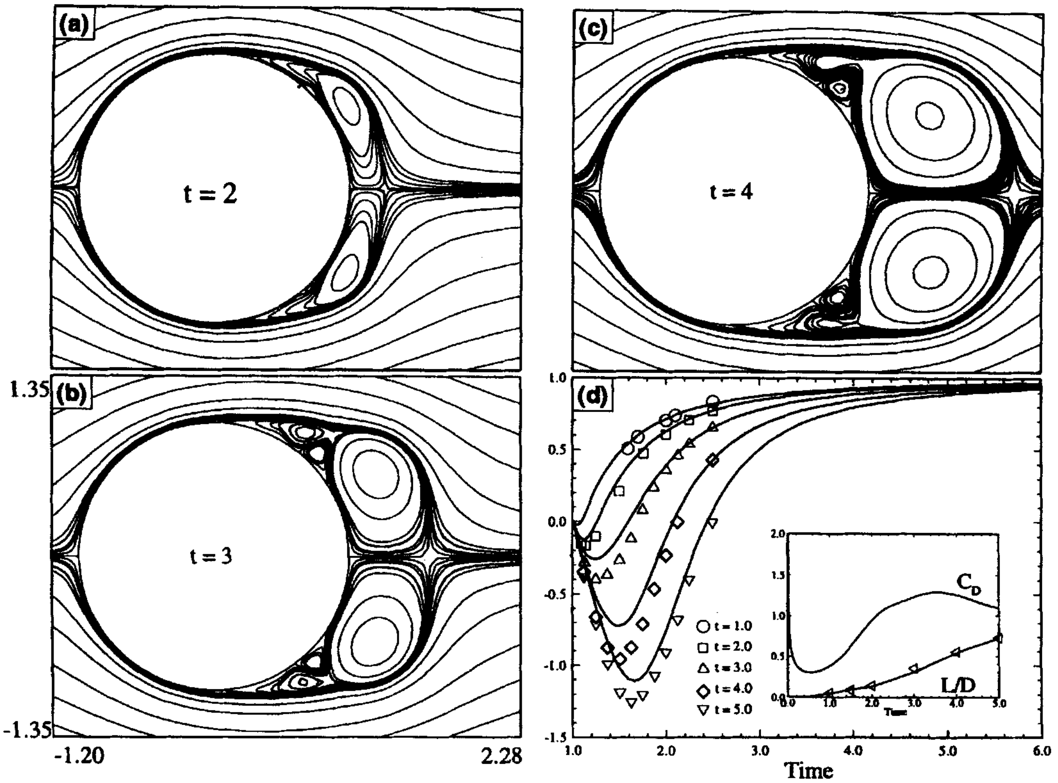

Figure 4. Early evolution of flow past an impulsively started circular cylinder at $R=3000$. (a)–(c) Streamline plots at $t=2, 3, 4$. (d) Radial velocity along symmetry axis behind cylinder at $t=1, 2, 3, 4, 5$. Shown in the inset are the drag coefficient (C_D) and wake length (L/D). ————, present; symbols, Reference 1

According to such a co-ordinate transformation, the boundary conditions (4) and (5) are written as (note that we suppress the t-variable for the moment)

$$\partial\psi/\partial\eta = \psi = 0 \quad \text{for } \eta = 0 \text{ and } -\Gamma \leqslant \xi \leqslant \Gamma, \tag{11}$$

$$\begin{gathered}\psi(-\Gamma,\eta) = \psi(\Gamma,\eta) \text{ and } \omega(-\Gamma,\eta) = \omega(\Gamma,\eta) \quad \text{for } 0 \leqslant \eta \leqslant \eta^*, \\ \text{where, in (7), } |z'(\zeta)| = \infty \text{ at } \zeta = \pm\Gamma + if(\eta^*),\end{gathered} \tag{12}$$

$$\psi(\pm\Gamma,\eta) = \psi^\circ(\pm\Gamma,\eta) \text{ and } \omega(\pm\Gamma,\eta) = 0 \quad \text{for } \eta^* \leqslant \eta \leqslant \eta_\infty, \tag{13}$$

$$\begin{gathered}\partial\psi/\partial\eta = \partial\psi^\circ/\partial\eta \text{ and } \omega \text{ is updated through (9) by the explicit Euler scheme} \\ \text{for } \eta = \eta_\infty \text{ and } -\Gamma \leqslant \xi \leqslant \Gamma.\end{gathered} \tag{14}$$

The outflow condition (14) has been shown to perform well in this work. Several arguments about optimizing the downstream boundary condition can be found in References 11 and 12.

3. THE FINITE DIFFERENCE SCHEME

First we deal with the transformed Poisson equation (10) together with the boundary conditions (11)–(14), in which we drop the condition $\partial\psi/\partial\eta = 0$ along the object's boundary. This no-slip condition will be respected later in conjunction with the wall vorticity generation.

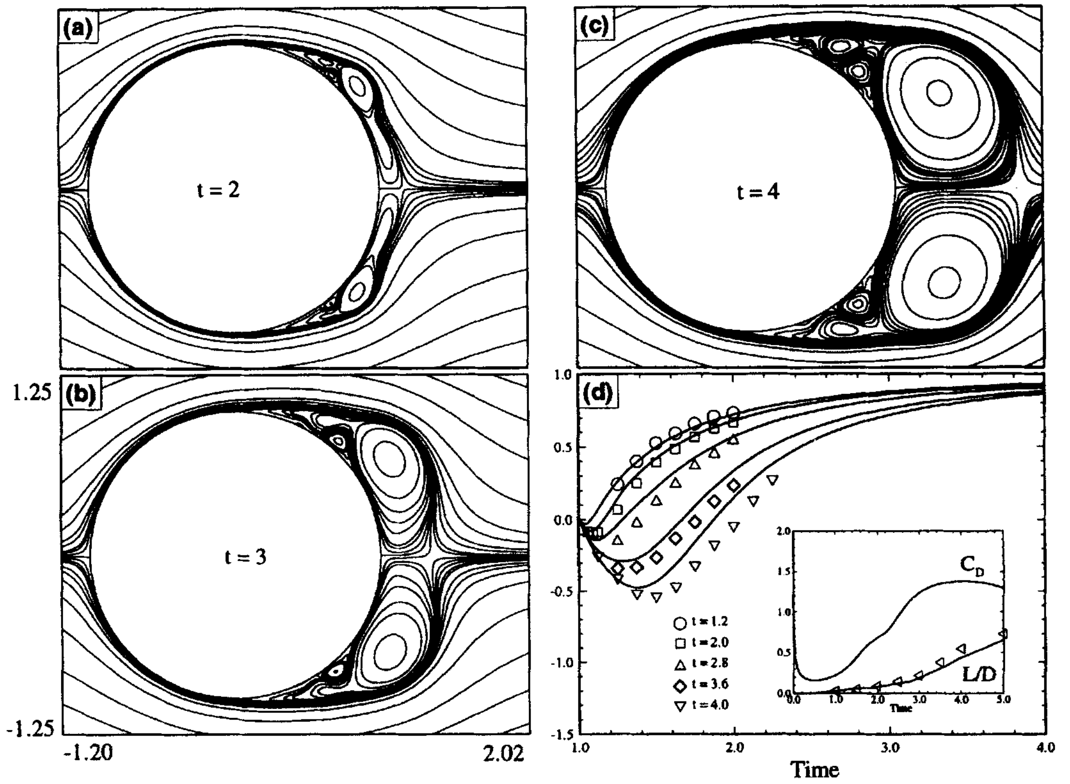

Figure 5. Early evolution of flow past an impulsively started circular cylinder at $R=9500$. (a)–(c) Streamline plots at $t=2$, 3, 4. (d) Radial velocity along symmetry axis behind cylinder at $t=1\cdot2$, 2, 2·8, 3·6, 4. Shown in the inset are the drag coefficient (C_D) and wake length (L/D). ————, present; symbols, Reference 1

Centred differencing is applied to discretize (10). The resultant system of algebraic equations is quite large for high-Reynolds-number flow. In order to attain a satisfactory rate of convergence, we employ a multigrid approach. The basic ingredients of our three-grid iterative method are a standard double-coarsening strategy on the grid, a five-point central difference formula for each grid, incomplete LU factorization as the smoothing operator and standard nine-point prolongation and restriction scheduled in a 'saw-tooth' manner. See Reference 13 for details of this framework.

Next we implement the no-slip condition $\psi_\eta = 0$ at $\eta = 0$. A common practice is to incorporate it into the approximation of $\psi_{\eta\eta}$ at $\eta = 0$ when one wants to estimate the wall vorticity. However, in the possible presence of high curvature along the object's boundary, such as $\lambda \ll 1$ in (1), it has been shown in our previous works[9,10] that a better alternative to respect this condition is the following projection approach.

Theorem 1

Let Ω be a neighbourhood around the object under consideration. The associated boundary $\partial\Omega = B_0 \cup B_1$ is equipped with a local co-ordinate system as shown in Figure 1. If ψ and ω are such that $\Delta\psi = -\omega$ in Ω and $\psi \equiv$ constant B_0, then the no-slip condition $\partial\psi/\partial v = 0$ on B_0 is equivalent to

$$\int_\Omega \omega g_n \mathrm{d}x\mathrm{d}y + \oint_{B_1}\left(g_n\frac{\partial\psi}{\partial v} - \psi\frac{\partial g_n}{\partial v}\right)\mathrm{d}\tau = 0 \quad \text{for } n = 0, 1, 2, \cdots, \tag{15}$$

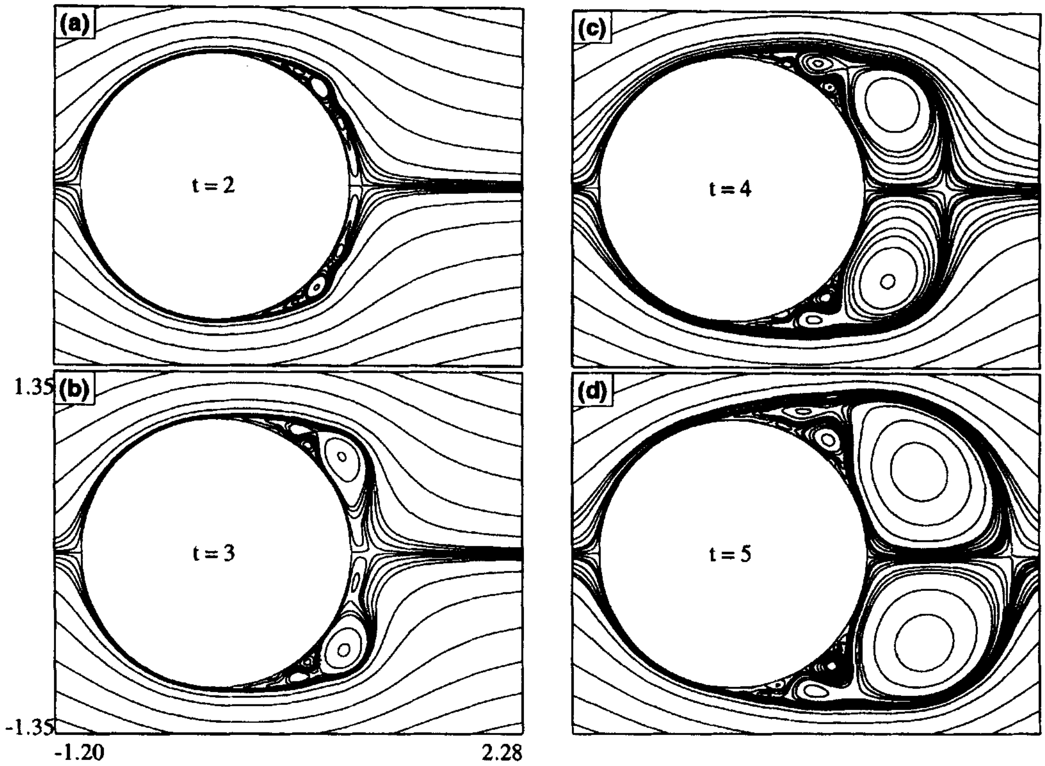

Figure 6. Early evolution of flow past an impulsively started circular cylinder at $R = 4 \times 10^4$. (a)–(d) Streamline plots at $t = 2, 3, 4, 5$

where the auxiliary functions g_n are given by the respective real and imaginary parts of $\exp[i\pi n(\zeta + \Gamma)/\Gamma)]$ via the co-ordinate transformation (1) and (7).

Using a numerical quadrature such as the trapezoidal rule, equation (15) can be put into the discrete (matrix) form

$$A_0 \cdot \omega_0 + A \cdot \omega + g \cdot \psi = 0. \qquad (16)$$

Note that the contribution of the wall vorticity ω_0 to the area integral is counted separately from that due to the interior vorticity ω. The reason for so doing is that in our approach the no-slip condition will be implemented as the introduction of a 'vortex-sheet' correction, given the interior vorticity and streamfunction merely satisfying the no-flux condition. Namely, we ask ω_0 to satisfy

$$\omega_0 = -A_0^{-1}(A \cdot \omega + g \cdot \psi). \qquad (17)$$

The matrix A_0 is composed of an orthogonal matrix representing the discrete Fourier transform and a diagonal matrix representing the local area elements along the line $\eta = 0$, i.e. the object's boundary. Thus the inverse A_0^{-1} can be obtained with ease and equation (17) just contains fully vectorizable matrix–vector multiplications.

Now we proceed to discretize the transformed vorticity transport equation (9). Spatial differentiations are all approximated by centred differencing as usual, except for the convection terms ω_ξ and ω_n appearing on the left-hand side of (9). To these terms the so-called convection

Table I. Summary of Reynolds number, grid size, extent of computational domain and time step

Re	Grid ($\xi \times \eta$)	*X*-min	*X*-max	*Y*-min	*Y*-max	Δt
1000	121 × 129	−11·37	96·92	−32·28	32·29	0·050
3000[a]	121 × 73	−11·37	18·14	−23·84	23·84	0·040
9500	181 × 89	−11·37	11·67	−20·60	20·60	0·025
4×10^4	241 × 193	−11·37	110·94	−32·70	32·70	0·010

[a] Early stage only

boundedness criterion (CBC) proposed by Gaskell and Lau[14] is applied in order to suppress the spurious oscillations brought about by the centred difference when the employed grid is not fine enough.

The basic idea behind the CBC is to improve from the finite volume point of view the well-known first-order upwind scheme in those situations where the related three nodal values of ω, say $(\omega_{i-2,j}, \omega_{i-1,j}, \omega_{i,j})$ or $(\omega_{i,j-2}, \omega_{i,j-1}, \omega_{i,j})$ used to predict the interfacial values $\omega_{i-1/2j}$ or $\omega_{i,j-1/2}$, are in the monotone regime. If the monotone condition holds, we try to recover the third-order

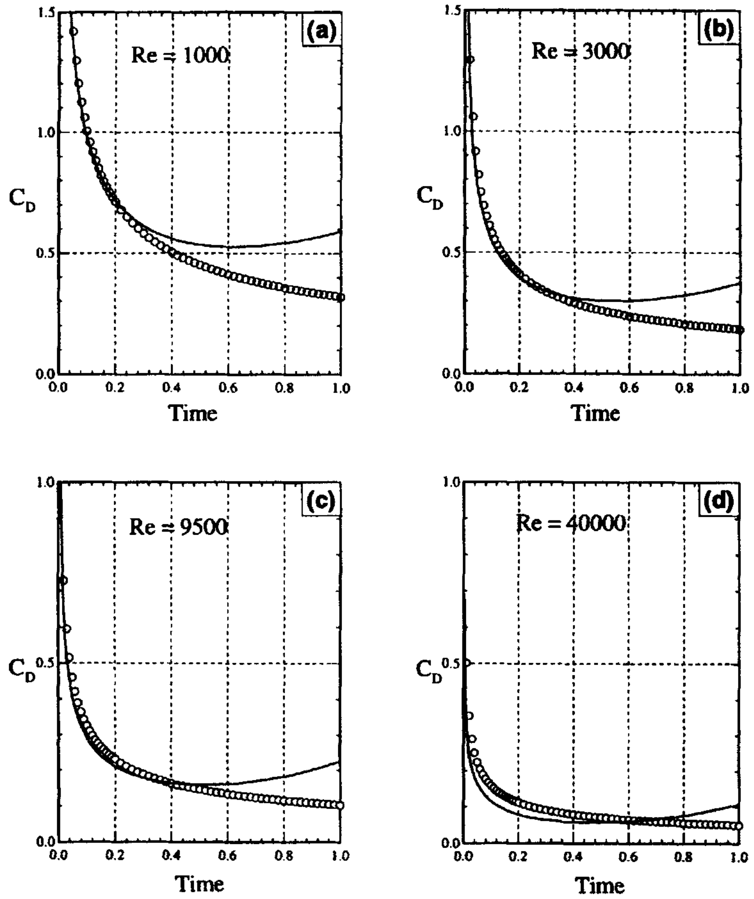

Figure 7. Early history of drag coefficient (C_D) for flow past a circular cylinder at $R =$ (a) 1000, (b) 3000, (c) 9500, (d) 4×10^4. ————, present; o, Reference 18

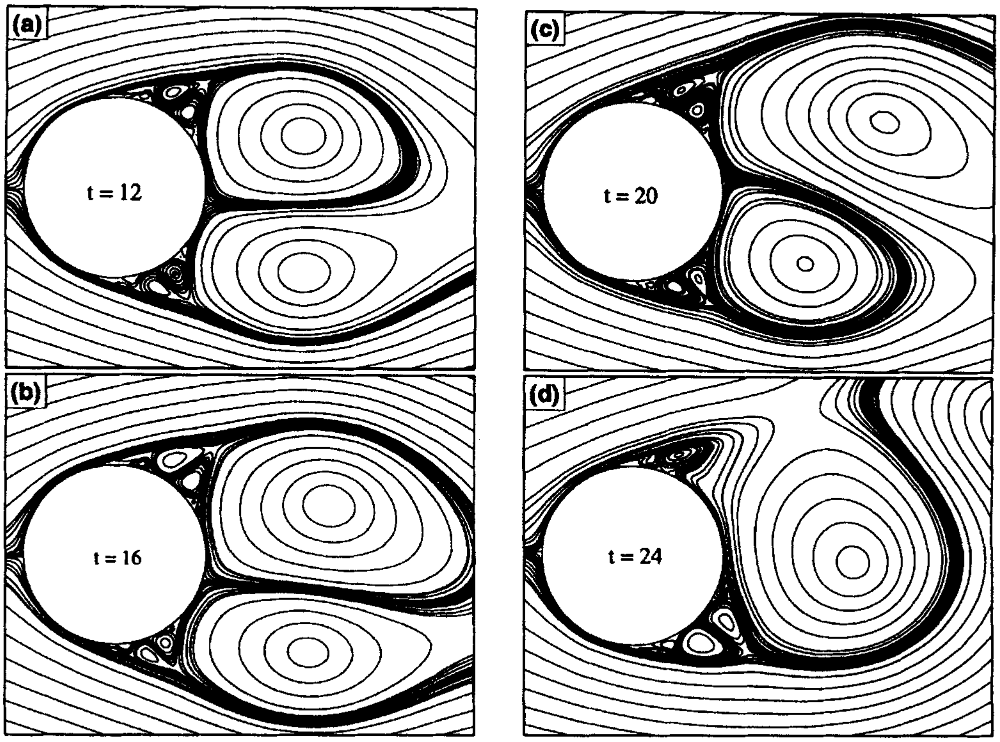

Figure 8. Symmetry breaking and onset of alternate vortex shedding for flow past a circular cylinder at $R = 4 \times 10^4$. (a)–(d) Streamline plots at $t = 12, 16, 20, 24$

accuracy of the QUICK scheme.[15] This effort amounts to constructing a function $y(x)$ in terms of a normalized variable x such that $0 \leqslant x \leqslant 1$, departing from the first-order upwind $y(x) = x$ to the QUICK scheme $y(x) = \frac{3}{8} + 3x/4$, under the constraints $x \leqslant y(x) \leqslant 1, y(0) = 0$ and $y(1) = 1$.

Various ways to construct such a function $y(x)$ have been discussed for example in References 14 and 16. We have noted that their respective merits are sometimes application-dependent. Although $y(x)$ is non-linear in general, one does not expect an involved expression. The following formula has been shown to be quite effective in our previous work:[10]

$$y_5(x) = 4x - 11x^2 + 18x^3 - 14x^4 + 4x^5, \quad 0 \leqslant x \leqslant 1. \tag{18}$$

Besides satisfying the aforementioned basic constraints, the function y_5 has the following features: (a) $y_5'(\frac{1}{2}) = y_5(\frac{1}{2}) = \frac{3}{4}$, i.e. tangent to the QUICK line at the crucial point $(\frac{1}{2}, \frac{3}{4})$; (b) $y_5'(1) = 0$, i.e. mimicking the cut-off of the QUICK interpolation near the right end in order to satisfy monotonicity.

Based on the above discussion, the discretized version of (9) is denoted by

$$J\omega_t + C(\psi, \omega_0, \omega) = (D_\xi + D_\eta)\omega. \tag{19}$$

In (19) the symbol $C(\cdot, \cdot, \cdot)$ denotes the convection term depending on ψ, ω_0 and ω in a non-linear manner; D_ξ and D_η are linear diffusion operators (including the coefficient 2/R) in directions ξ and η respectively. Note that the boundary conditions (11)–(14), other than specifying the wall vorticity ω_0 can be discretized with ease and hence will be skipped for simplicity of expression.

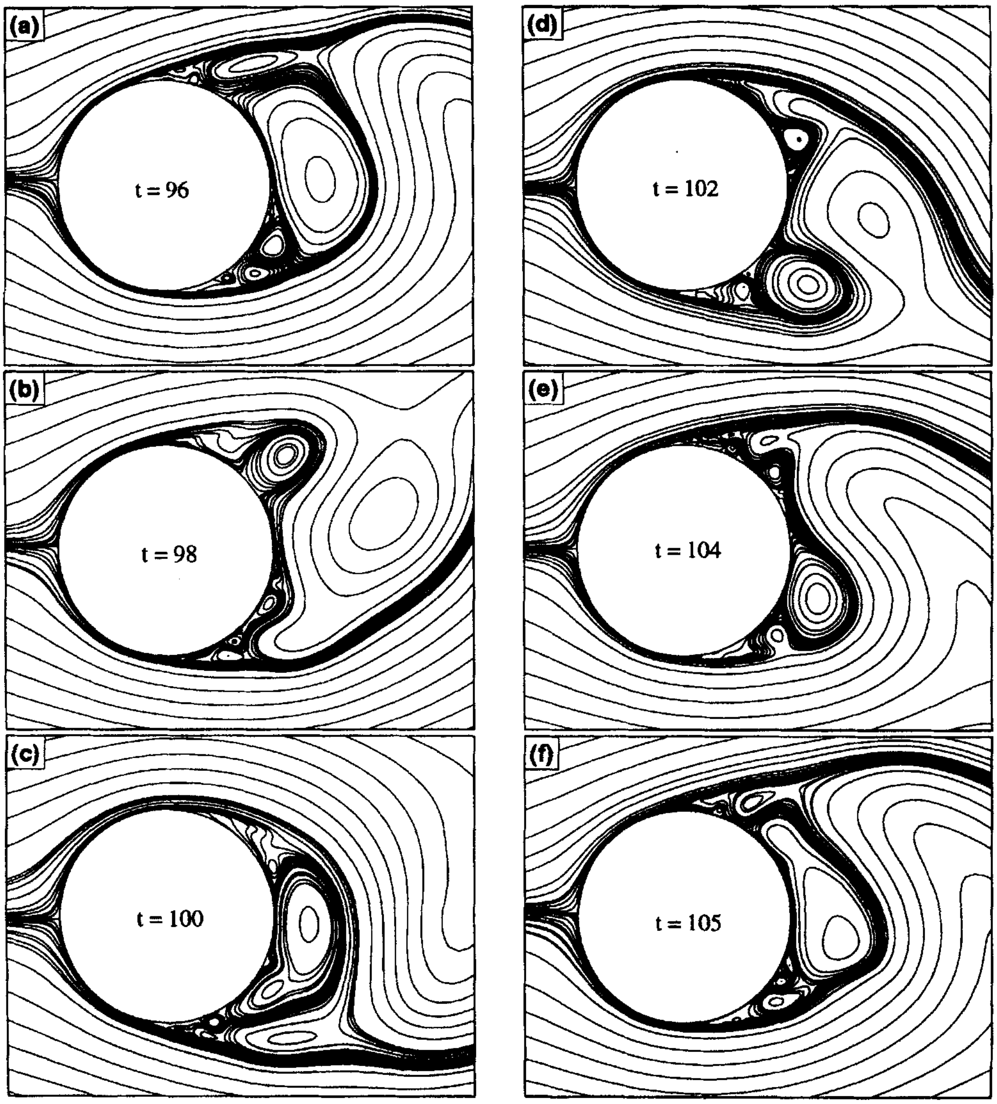

Figure 9. Cycle of alternate vortex shedding for fully developed flow past a circular cylinder at $R = 4 \times 10^4$. (a)–(f) Streamline plots at $t = 96, 98, 100, 102, 104, 105$

According to (19), the advancement of the interior vorticity ω, and ψ and ω_0 in turn, from time t^n to t^{n+1} with a time step Δt is summarized as follows. Note that the superscripts attached to ψ, ω_0, ω, etc. indicate the time dependence of these data.

Algorithm A

A1. Given ω^n, solve (10) for ψ^n with the proposed multigrid scheme. Then place ω^n and ψ^n into (17) to get ω_0^n.

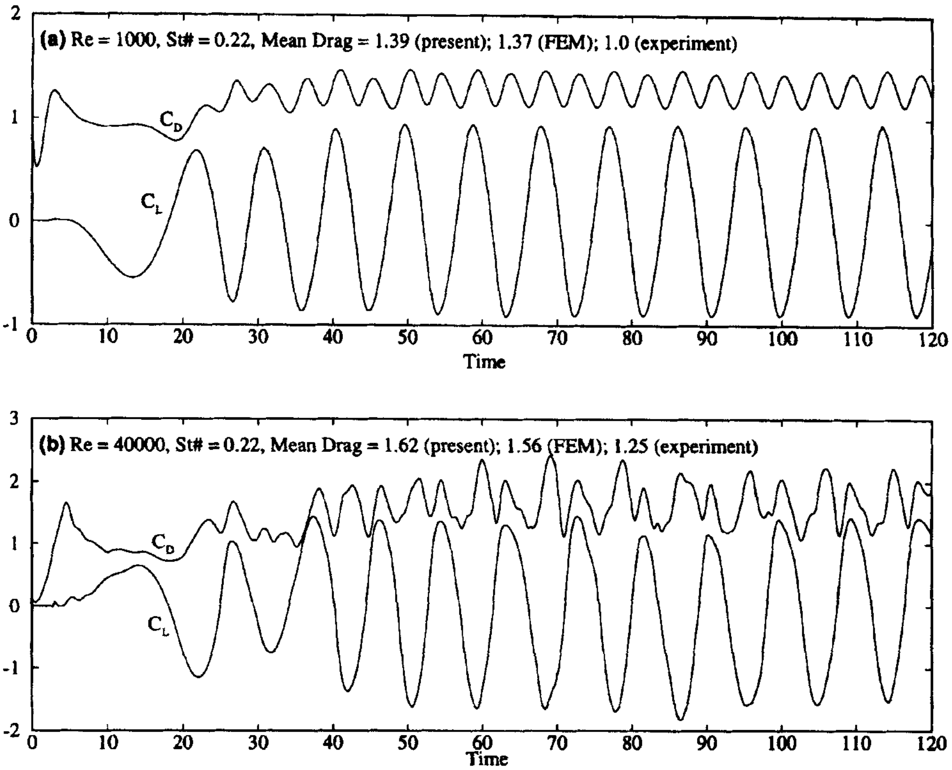

Figure 10. Long-term history of drag (C_D) and lift (C_L) coefficients for flow past a circular cylinder at R = (a) 1000, (b) 4×10^4

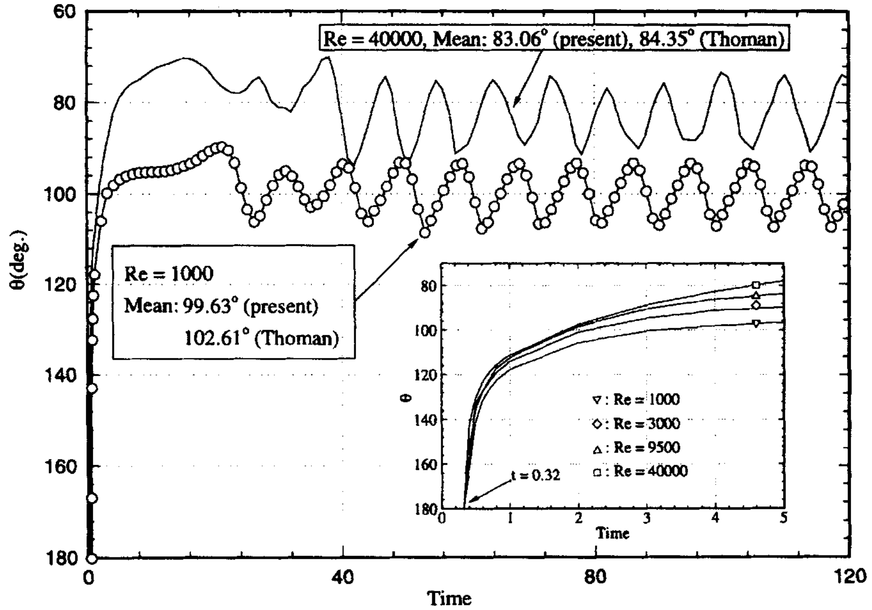

Figure 11. Long-term history of forward separation angle for flow past a circular cylinder at $R = 1000$ (-o-) and 4×10^4 (————). Shown in the inset are the early results for $R = 1000$ (▽), 3000 (◇), 9500 (△), 4×10^4 (□)

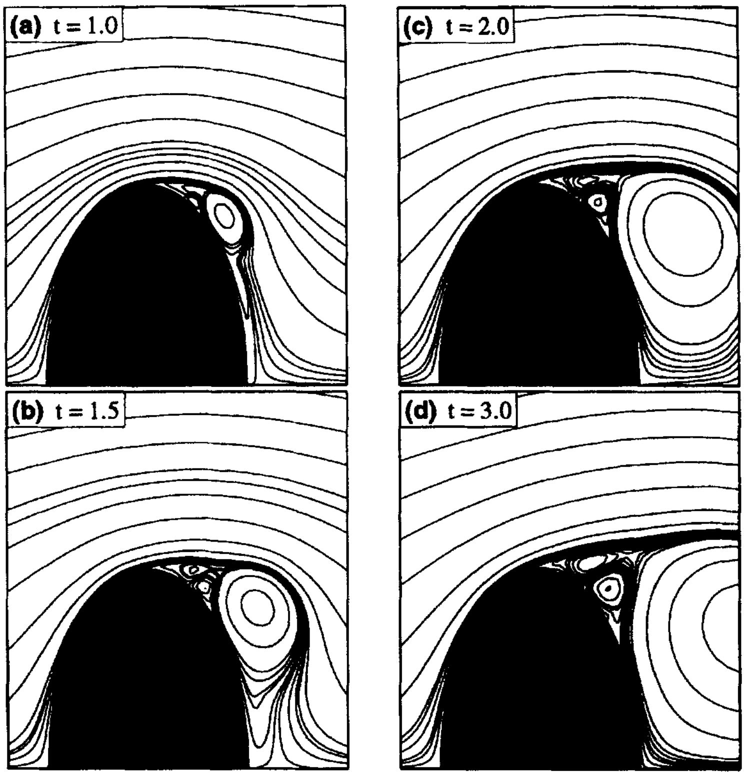

Figure 12. Streamlines of flow past an impulsively started elliptical cylinder with $(\lambda, \Theta) = (0{\cdot}5, 90°)$ at $R = 9500$. (a)–(d) Early evolution from β- to α-phenomenon at $t = 1$, 1·5, 2, 3

A2. Compute $C^n \equiv C(\psi^n, \omega_0^n, \omega^n)$ with the proposed CBC scheme and $D^n \equiv (D_\xi + D_\eta)\omega^n$ in which ω_0^n is used.

A3. Define $\mu = \Delta t/2J$. Apply the vectorized Thomas algorithm[17] twice to solve

$$(I - \mu D_\xi) \cdot (I - \mu D_\eta)\tilde{\omega} = \mu(D^n - C^n) \tag{20}$$

for $\tilde{\omega}$, with the wall boundary condition $\tilde{\omega}_0 \equiv 0$.

A4. Set $\omega^{n+1/2} = \omega^n + \tilde{\omega}$. Then repeat step A1 with superscript $n + \frac{1}{2}$ instead.

A5. Compute $C^{n+1/2} \equiv C(\psi^{n+1/2}, \omega_0^{n+1/2}, (1-\beta)\omega^n + \beta\omega^{n+1/2})$ with the proposed CBC scheme again. The parameter β is such that $0 \leqslant \beta \leqslant 1$.

A6. Apply the vectorized Thomas algorithm twice again to solve

$$(I - \mu D_\xi) \cdot (I - \mu D_\eta)\tilde{\omega} = 2\mu(D^n - C^{n+1/2}) \tag{21}$$

for $\tilde{\omega}$, with the wall boundary condition $\tilde{\omega}_0 = \gamma(\omega_0^{n+1/2} - \omega_0^n)$. The parameter γ is such that $0 \leqslant \gamma \leqslant 2$.

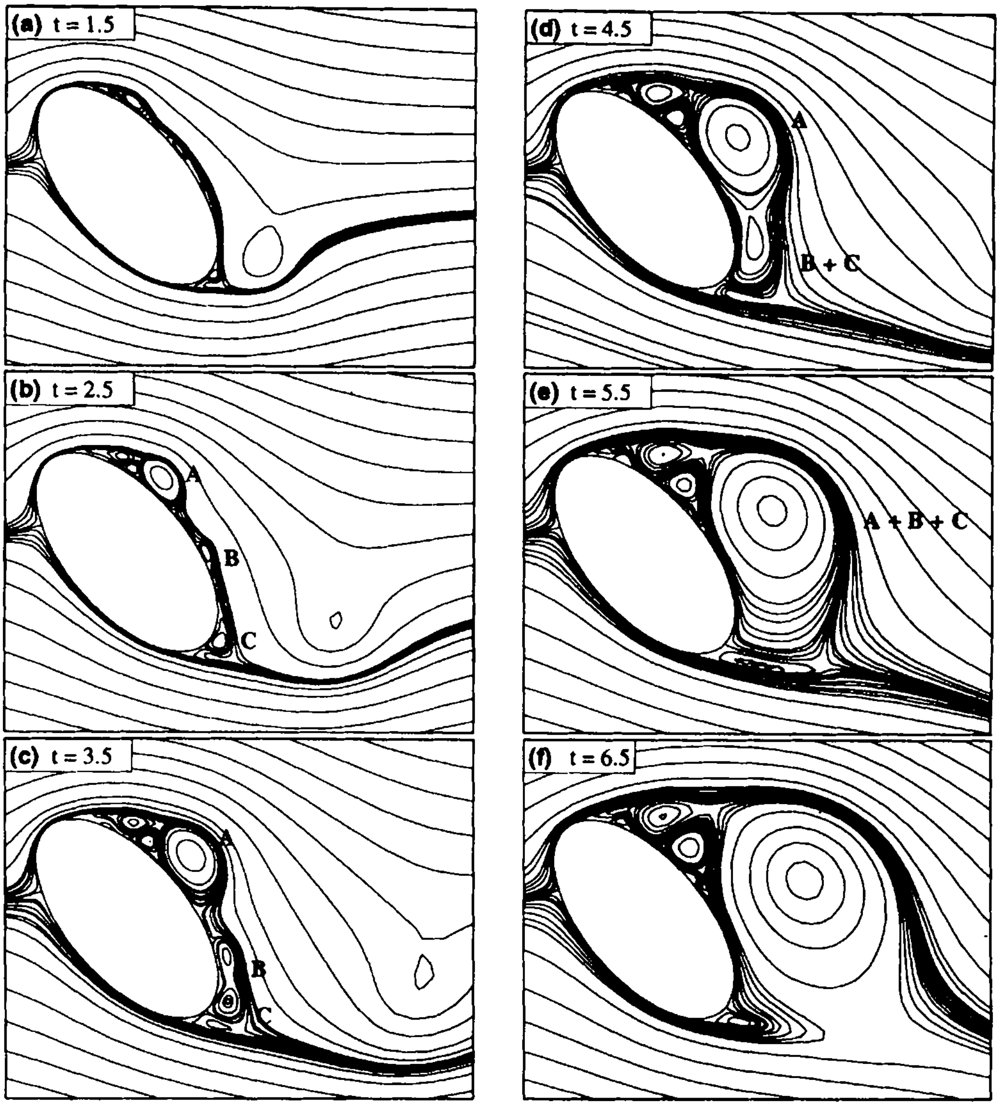

Figure 13. Strealines of flow past an impulsively started elliptical cylinder with (λ, Θ) = (0·5, 50°) at $R = 9500$. (a)–(f) Early development of wake behind the cylinder at t = 1·5, 2·5, 3·5,4·5, 5·5,6·5

A7. Set $\omega^{n+1} = \omega^n + \tilde{\omega}$ and complete the algorithm for one time step. To continue, go back to step A1.

Note that two relaxation parameters β and γ are introduced in Algorithm A. If $\beta = 1$ and $\gamma = 2$, this algorithm corresponds to applying the midpoint rule to the convection part and the Crank–Nicolson scheme to the diffusion part. Therefore a second-order formal accuracy in time is attained. However, we find that the corresponding stability is not as good as we want, since the allowable time step is too

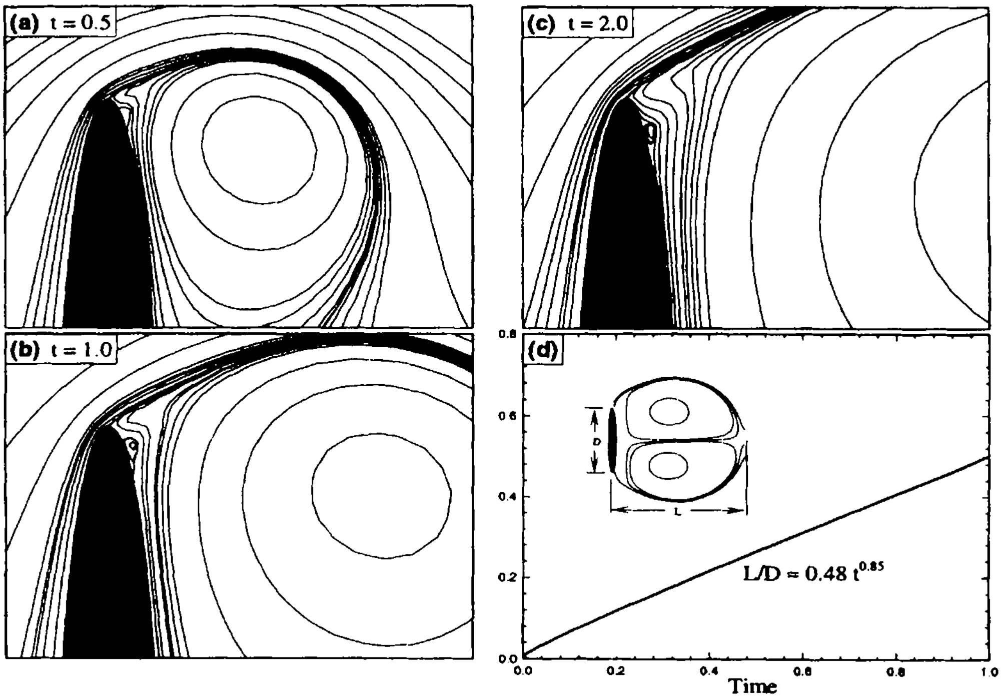

Figure 14. Strealines of flow past an impulsively started elliptical cylinder with $(\lambda, \Theta) = (0{\cdot}1, 90°)$ at $R = 1000$. (a)–(c) Early development of wake behind top tip of cylinder at $t = 0{\cdot}5$, 1, 2. (d) Early growth of main wake length (L/D) against time

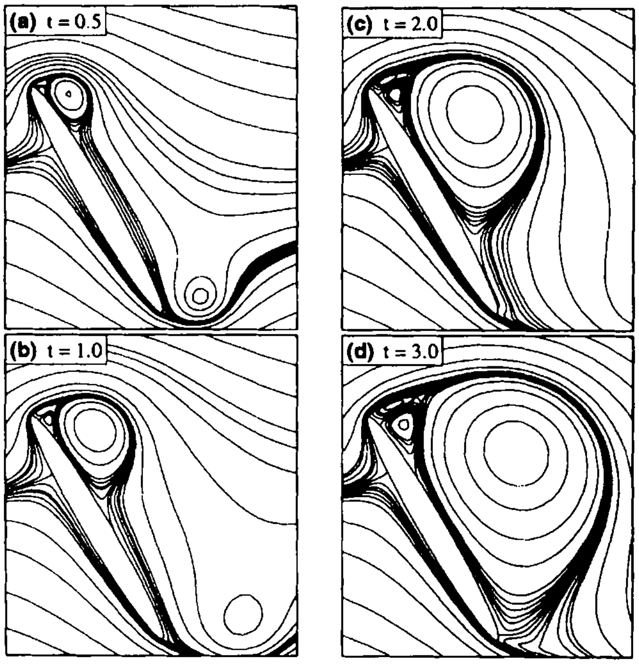

Figure 15. Streamlines of flows past an impulsively started elliptical cylinder with $(\lambda, \Theta) = (0{\cdot}1, 60°)$ at $R = 1000$. (a)–(d) Early development of wake behind cylinder at $t = 0{\cdot}5$, 1, 2, 3

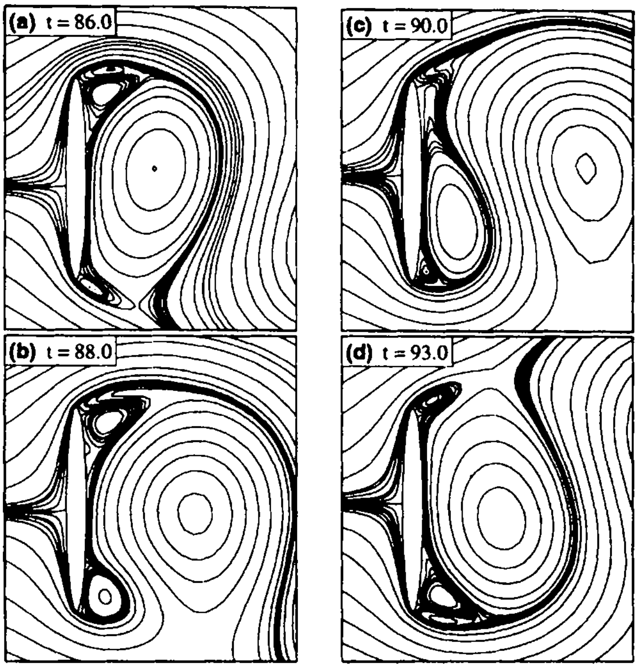

Figure 16. Streamlines of fully developed flow past an elliptical cylinder with $(\lambda, \Theta) = (0{\cdot}1, 90°)$ at $R = 1000$. (a)–(d) Near-wake structure along with alternate vortex shedding at $t = 86, 88, 90, 93$

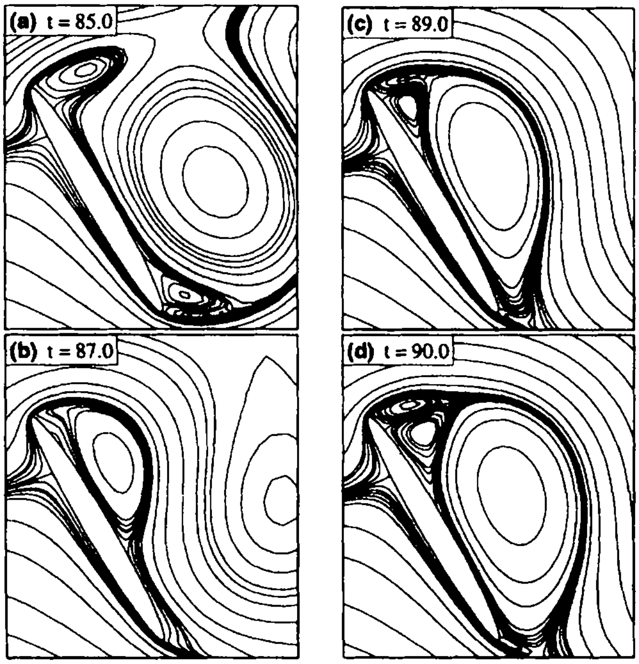

Figure 17. Streamlines of fully developed flow past an elliptical cylinder with $(\lambda, \Theta) = (0{\cdot}1, 60°)$ at $R = 1000$. (a)–(d) Near-wake structure along with alternate vortex shedding at $t = 85, 87, 89, 90$

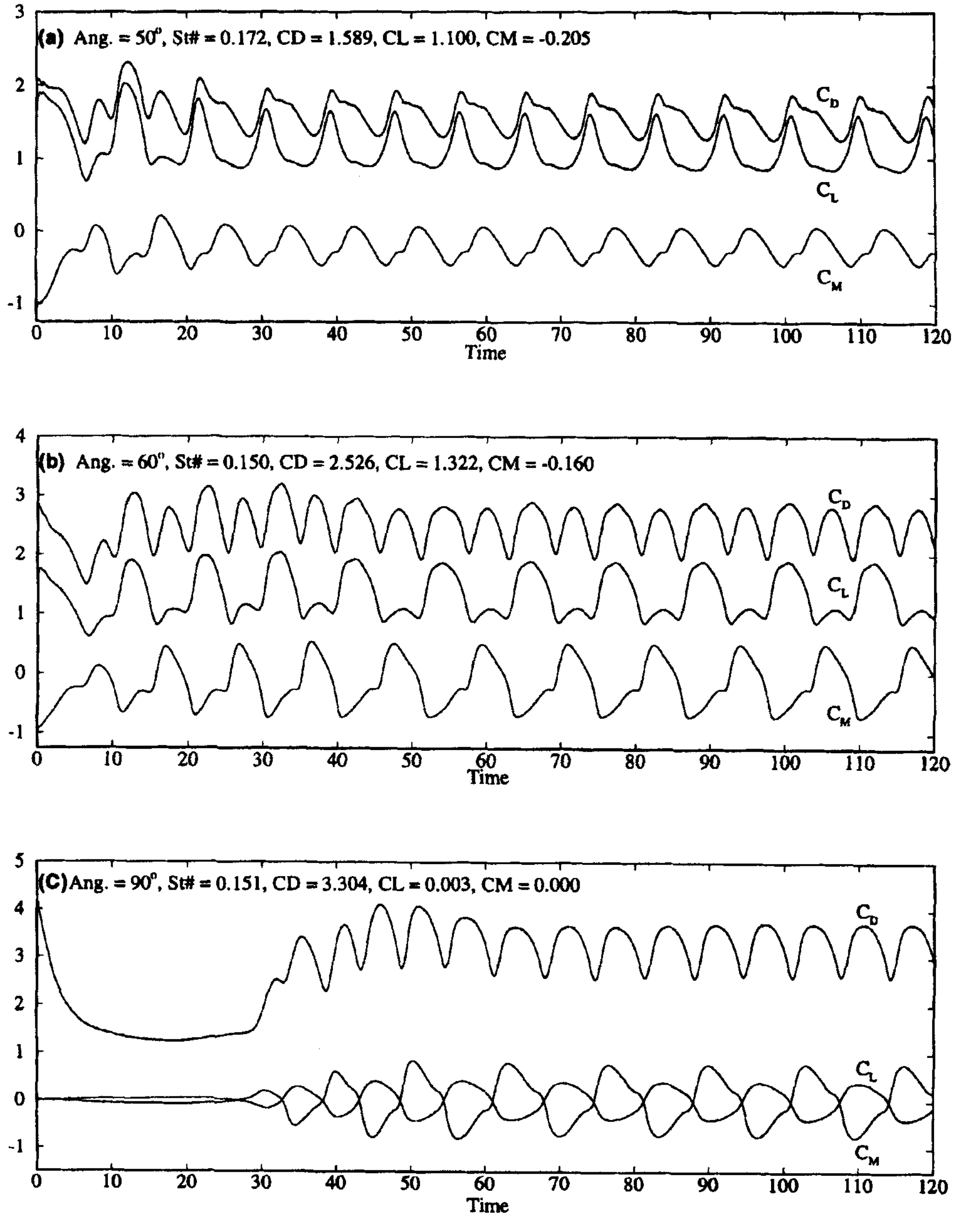

Figure 18. Long-term history of drag (C_D), lift (C_L) and moment (C_M) coefficients for flow past an elliptical cylinder with $\lambda = 0{\cdot}1, R = 1000$. Angle of attack $\Theta =$ (a) 50°, (b) 60°, (c) 90°

small to perform long-term simulations. A simple remedy, at the sacrifice of formal accuracy, is to relax β and $\gamma(\beta = \gamma = 0{\cdot}8$, say). Significant improvement in stability has been observed by this procedure.

In view of (20) and (21) the matrices related to $I - \mu D_\xi$ and $I - \mu D_\eta$ are time-independent if Δt is fixed. Therefore a more efficient use of the Thomas algorithm is achieved in comparison with ADI schemes.[17] We shall term Algorithm A a semi-explicit scheme.

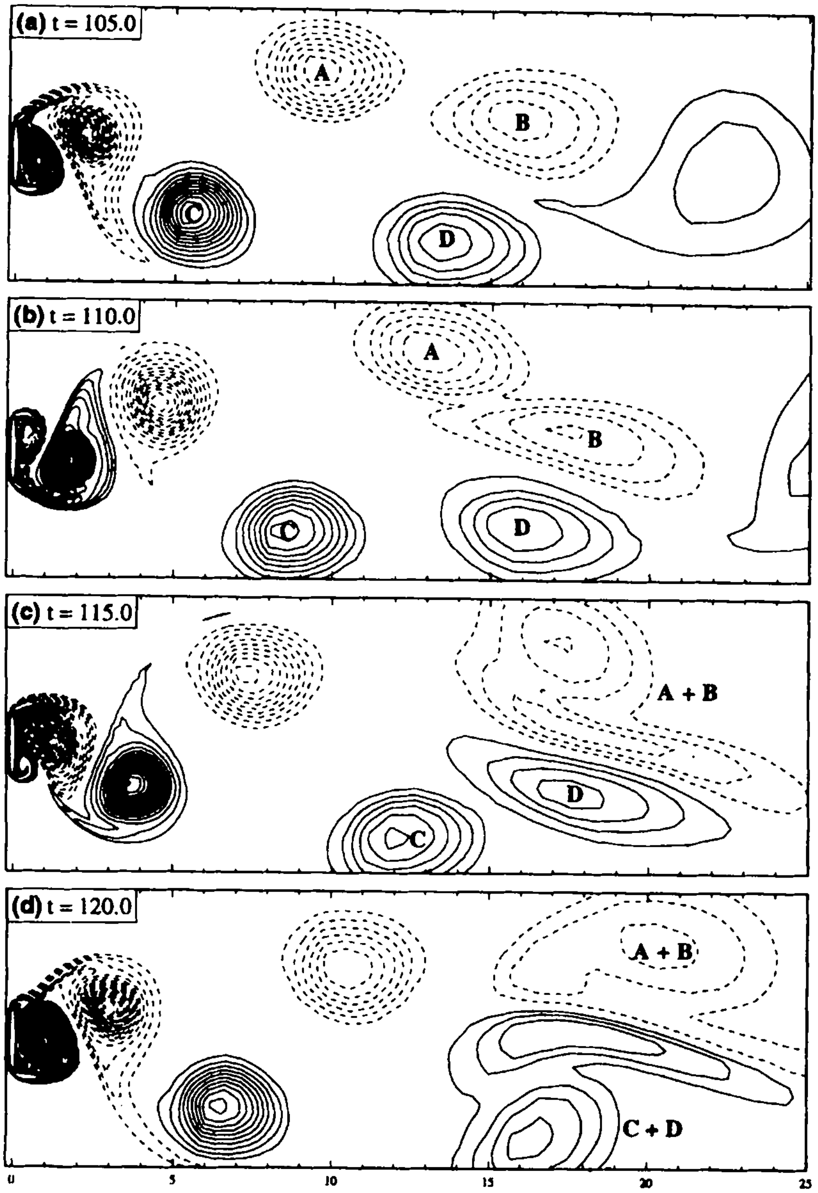

Figure 19. Vorticity contours for fully developed flow past an elliptical cylinder with $(\lambda, \Theta) = (0{\cdot}1, 90^\circ)$ at $R = 1000$. (a)–(d) Snapshots at $t = 105$, 110, 115, 120

During the simulation an important output is the fluid dynamic quantities such as drag, lift and moment. For high-Reynolds-numbers flow the essential part of each quantity is due to the surface pressure and is calculated by the following thereom which has been shown in our previous works[9,10] to yield smoother results than those yielded by the conventional approach.

Theorem 2

Let Ω, B_0 and B_1 be as shown in Theorem 1 and let ω and ψ denote the vorticity and streamfunction respectively. Then the drag, lift and moment exerted by the non-dimensional surface pressure can be expressed as

$$\frac{\mathrm{d}}{\mathrm{d}t}\oint_{B_1}\psi\frac{\partial\varphi}{\partial\nu}+\int_{\Omega}\omega\frac{\partial(\psi,\varphi)}{\partial(x,y)}\mathrm{d}x\mathrm{d}y+\frac{2}{R}\left(\oint_{B_1}\omega\frac{\partial\varphi}{\partial\nu}-\oint_{B_0}\omega\frac{\partial\varphi}{\partial\nu}\right). \tag{22}$$

The auxiliary function φ in (22) satisfies the partial differential equation

$$\varphi_{xx}+\varphi_{yy}=0 \quad \text{in } \Omega, \qquad \varphi=0 \quad \text{on } B_1, \qquad \varphi=g \quad \text{on } B_0, \tag{23}$$

where $g(x,y)=-y$ for drag, x for lift and $(x^2+y^2)/2$ for moment.

The skin friction part of these quantities is handled as usual:

$$(\text{drag, lift, moment})_{\mathrm{S}}=\frac{2}{R}\oint\omega(\mathrm{d}x,\mathrm{d}y,x\mathrm{d}y-y\mathrm{d}x). \tag{24}$$

Note that the closed integral is done counterclockwise. The drag, lift and moment coefficients are defined as

$$(C_{\mathrm{D}},C_{\mathrm{L}})=(\text{drag, lift})/\tfrac{1}{2}\rho U_\infty^2 D, \qquad C_{\mathrm{M}}=\text{moment}/\tfrac{1}{4}\rho U_\infty^2 D^2. \tag{25}$$

In the denominators (25), ρ, U_∞ and D stand for the fluid density, the flow speed at infinity and the diameter of the physical object respectively. The long-term history of these coefficients can be used to assist the estimation of vortex-shedding frequency, if it occurs. The Strouhal number St is defined as

$$St=\text{frequency}\ \cdot \mathrm{D}\cdot\sin\Theta/\mathrm{U}_\infty, \tag{26}$$

where Θ denotes the angle of attack. Note again that Θ is input in degrees with a tacit conversion to radians. By convention, $\Theta=90°$ for flow past a circular cylinder.

For the initial flow field over a circular cylinder the following analytic result adapted from Reference 18 is used to check the accuracy of our numerical results:

$$C_{\mathrm{D}}=4\surd(2\pi/Rt)+2\pi(9-15/\surd\pi)/R, \quad 0<t<1. \tag{27}$$

4. WORKED EXAMPLES AND DISCUSSON

We begin with the *de facto* standard test of flow past a circular cylinder. For Reynolds number R up to 10^4 there exist several oft-cited numerical and physical experiments in the literature, although most results are merely concerned with the early-stage development. In what follows, we shall report both the early-stage and the long-term simulations for $R=1000$, 3000, 9500 and 4×10^4. A Convex C3420 vector computer was used.

Figure 2 presents a sketch of our prowake, orthogonal grid system. Shown in Table 1 are the grid ($\xi\times\eta$) size, the extent of the computational domain and the time step (Δt) we used in conjunction with different value of R. The cylinder is centred at (0, 0) and is of radius unity. Along with our simulation of the early-stage flow development the reference data are mainly from References 1, 2 and 6. In view of Table I the time step associated with our semi-explicit scheme is comparable with that using ADI and backward Euler schemes.[1,3]

Figures 3(a)–3(c) present the evolution of streamline patterns for flow at $R = 1000$. We did not assume any symmetry condition on flow problems related to a circular cylinder, although it more or less appears so. The evolution from a pair of main eddies to the so-called α-phenomenon[1] is clearly shown. Figure 3(d) presents the radial velocity along the symmetry axis behind the cylinder at dimensionless times $t = 1, 2, 3, 4$ and 5. Shown in the inset are the corresponding drag coefficient (C_D) and wake length (L/D). Symbols in this figure stand for the reference data from Reference 6. Similar time evolution for flow at $R = 3000$ is shown in Figures 4(a)–(d), but with reference data from Reference 1.

Figures 5(a)–5(c) present the streamline patterns for flow at $R = 9500$. The evolution from the so-called β-phenomenon[1] to a pair of main eddies plus a multiplication of secondary vortices is clearly shown. Figure 5(d) presents the radial velocity along the symmetry axis behind the cylinder at dimensionless times $t = 1{\cdot}2, 2{\cdot}0, 2{\cdot}8, 3{\cdot}6$ and 4·0. Shown in the inset are the corresponding drag coefficient (C_D) and wake length (L/D). Symbols in this figure stand for reference data from Reference 1. Such a type of time evolution is more prominent for flow at $R = 4 \times 10^4$, as shown in Figures 6(a)–6(d).

According to these demonstrations, a good agreement either with physical experiments[1] or with higher-order-accurate numerical solutions[2,6] is established. A further check is presented in Figures 7(a)–7(d), in which the early history of the drag coefficient (C_D) is compared with the analytic result (27) from Reference 18. Again a good agreement is established.

Next we proceed to the long-term simulation. The rather symmetric evolution of the flow patterns as shown in Figures 3–6 will continue for a long while before breakdown due to the wake instability. After that it evolves into a pattern of alternate vortex shedding. Figures 8(a)–8(d) show the outset of this phenomenon for flow at $R = 4 \times 10^4$, while Figures 9(a)–9(f) show a fully developed case.

Figures 10(a) and 10(b) present the long-term history of the drag and lift coefficients for flow at $R = 1000$ and 4×10^4 respectively. The computed Strouhal numbers, 0·22 for both cases, are in good agreement with the value 0·21 extrapolated from the following empirical formula of Roshko:[19]

$$St = 0{\cdot}212(1 - 21{\cdot}2/R), \quad 50 < R < 150. \tag{28}$$

The mean drag coefficients (1·39 and 1·62 for $R = 1000$ and 4×10^4 respectively) are similar to those obtained by a high-order-accurate finite element method (1·37 and 1·56 respectively,[20] but larger than the experimental values (1·0 and 1·25 respectively).[21] Such a discrepancy is due to the two-dimensional, laminar simulation failing to represent the growth of turbulence in the wake.

Figure 11 presents the long-term history of the forward separation angle where the surface vorticity underwent the first sign change away from the front stagnation point (180° means the rear stagnation point) for flow at $R = 1000$ and $4 \times 10.^4$ The early history is blown up in the inset. The computed mean separation angles (99·6° and 83·1° respectively) are consistent with the results (102·6° and 84·4° respectively) of Thoman and Szewczyk,[4] but we observe a more prominent (regular) oscillation ($\sim \pm 6°$ for $R = 1000$, $\sim \pm 8°$ for $R = 4 \times 10^4$) in respect to the alternate vortex shedding. We believe that this is a correction to that observed by the first-order upwinding in Reference 4.

According to these demonstrations, a good performance of our scheme in long-term simulation is also established for flow past a circular cylinder. In the following we shall show a number of tests on flow past an elliptical cylinder in which the aspect ratio (λ) and the angle of attack (Θ) are the two controlled parameters.

Figures 12(a)–12(d) present the early-stage development of flow past an elliptical cylinder with $(\lambda, \Theta) = (0{\cdot}5, 90^\circ)$ at $R = 9500$. Again the evolution from the β- to the α-phenomenon is clearly shown. If the cylinder is oblique to the incoming flow, say $\Theta = 50^\circ$, we observe the time evolution from a pseudo-β-phenomenon to a sequence of vortex merging (as indicated by A, B and C) to a main wake plus a multiplication of secondary vortices taking place behind the leading edge, along with the first vortex shedding from the trailing edge, see Figures (13a)–13(f).

Note that as the aspect ratio (λ) is decreased, high curvature is present along the cylinder and forms a challenge to numerical stability in terms of the allowable time step (Δt). This is because the related Jacobian $J \ll 1$ in (19). Owing to the limitation on computer resources, we shall reduce the Reynolds number in the remaining demonstrations.

Figure 14(a)–14(c) present the early stage of flow past an elliptical cylinder with $(\lambda, \Theta) = (0{\cdot}1, 90^\circ)$ at $R = 1000$. The associated time step is $\Delta t = 1{\cdot}25 \times 10^{-3}$. Unlike the flow past a circular cylinder, we merely observe the growth and decay of an isolated secondary eddy behind either tip of the ellipse. Meanwhile, the growth of the main eddy is much faster than that behind a circular cylinder. As shown in Figure 14(d), the early time evolution of the wake length (L/D) is approximately of the form

$$L/D \approx 0{\cdot}48 t^{0{\cdot}85}, \quad 0 < t < 1. \tag{29}$$

The scene of a main eddy plus a pair of secondary vortices (mimicking the α-phenomenon) is observed when the angle of attack is other than 90°. Figures 15(a)–15(d) show such an evolution behind the leading edge of an elliptical cylinder with $\Theta = 60^\circ$, along with the first vortex shedding from the trailing edge.

On the other hand, such a pseudo-α-phenomenon is observed to appear alternately behind the tips of the elliptical cylinder for fully developed flow at a rather arbitrary angle of attack. This is evidenced in Figures 16(a)–16(d) and 17(a)–17(d).

Figures 18(a)–18(c) present the long-term history of the drag, lift and moment coefficients for flow past an elliptical cylinder with $\lambda = 0{\cdot}1$ and $\Theta = 50^\circ, 60^\circ$ and 90° respectively at $R = 1000$. The respective Strouhal numbers St, as defined in (26), are $0{\cdot}172, 0{\cdot}150$ and $0{\cdot}151$. For $\Theta \leqslant 50^\circ$ this number is similar to that obtained for $R \leqslant 400$ by Chou[9] and Lugt and Haussling.[5] For $\Theta \geqslant 60^\circ$ we see that this number agrees with the wind tunnel experiment ($0{\cdot}148 \pm 0{\cdot}003$) of flow past a flat plate (i.e. $\lambda = 0$) by Fage and Johansen.[22] For the 90° case the mean drag coefficient ($3{\cdot}30$) is also comparable with a recent numerical result ($\sim 3{\cdot}7$) of flow past a flat plate by Najjar and Vanka.[23] These values are again much larger than the experimental value (~ 2)[22] owing to the assumption of two-dimensionality.

Finally, Figures 19(a)–19(d) present several stages of overall vorticity contours for flow past a normal thin cylinder (i.e $\lambda = 0{\cdot}1, \Theta = 90^\circ$) at $R = 1000$. It shows that a regular spacing among shedded vortices occurs in the near wake only. Complex vortex interactions such as merging or pairing between vortices of like sense (indicated in Figure 19 by A + B and C + D respectively) are observed in the far wake. These observations might be too crude owing to the numerical viscosity introduced in the far wake. A refinement can be drawn from the well-resolved simulations of Reference 23 for flow past a normal plate, but it is too expensive to perform by our computing facilities.

5. CONCLUSIONS

We have proposed a semi-explicit finite difference scheme to simulate unsteady two-dimensional flow past a bluff object at high Reynolds number. In conjunction with the streamfunction–vorticity formulation of the Navier–Stokes equations, the interior vorticity, streamfunction and wall vorticity are updated in turn for each time step. Such a decoupling results in an efficient use of multigrid and vectorization techniques. The numerical performance of this scheme has been shown to be comparable with that of other more sophisticated methods.

ACKNOWLEDGEMENTS

This research work was supported in part by the National Science Council under grants NSC84-2121-M-001-023 and NSC84-2112-M-001-052.

REFERENCES

1. R. Bouard and M. Coutanceau, 'The early stage of development of the wake behind an impulsively started cylinder for $40 < Re < 10^4$, *J. Fluid Mech.*, **101**, 583–607 (1980).
2. Ta Phuoc Loc and R. Bouard, 'Numerical solution of the early stage of the unsteady viscous flow around a circular cylinder: a comparison with experimental visualization and measurements', *J. Fluid Mech.*, **160**m 93–117 (1985).
3. T. Kawamura and K. Kuwahara, 'Computation of high Reynolds number flow around a circular cylinder with surface roughness', *AIAA Paper 84-0340*, 1984.
4. D. C. Thoman and A. A. Szewczyk, 'Time-dependent viscous flow over a circular cylinder', *Phys. Fluids Suppl. II*, **12**, 76–86 (1969).
5. H. J. Lugt and H. J. Haussling, 'Laminar flow past an abruptly accelerated elliptic cylinder at 45° incidence', *J. Fluid Mech.*, **65**, 711–734 (1974).
6. Ta Phuoc Loc, 'Numerical analysis of unsteady secondary vortices generated by an impulsively started circular cylinder', *J. Fluid Mech.*, **100**, 111–128 (1980).
7. V. A. Patel, 'Flow around the impulsively started elliptic cylinder at various angles of attack', *Comput. Fluids*, **9**, 435–462 (1981).
8. K. N. Ghia, U. Ghia, G. A. Osswald and C. A. Liu, 'Simulation of separated flow past a bluff body using Navier–Stokes equations', in F. T. Smith and S. N. Brown (eds), *Boundary-Layer Separation, IUTAM Symp.*, Springer, Berlin, 1987, pp. 251–267.
9. M. H. Chou, 'An efficient scheme for unsteady flow past an object with boundary conformal to a circle', *SIAM J. Sci. Stat. Comput.*, **13**, 860–873 (1992).
10. M. H. Chou, 'Simulation of slightly viscous external flow by a grid–particle domain decomposition method', *Comput. Fluids*, **24**, 333–347 (1995).
11. J. Y. Sa and K. S. Chang, 'On far-field streamfunction condition for two-dimensional incompressible flows', *J. Comput. Phys.*, **91**, 398–412 (1990).
12. M. Behr, J. Liou, R. Shih and T. E. Tezduyar, 'Vorticity–streamfunction formulation of unsteady incompressible flow past a cylinder: sensitivity of the coupled flow field to the location of the outflow boundary', *Int. j. numer. methods fluids*, **12**, 323–342 (1991).
13. P. Sonneveld, P. Wesseling and P. M. de Zeeuw, 'Multigrid and conjugate gradient methods as convergence acceleration techniques', in D. J. Paddon and H. Holstein (eds), *Multigrid Methods for Integral and Differential Equations*, Clarendon, Oxford, 1985, pp. 117–167.
14. P. H. Gaskell and A. K. Lau, 'Curvature-compensated transport: SMART, a new boundedness-preserving transport algorithm', *Int. j. numer. methods fluids*, **8**, 617–641 (1988).
15. B. P. Leonard, 'A stable and accurate convective modelling procedure based on quadratic upstream interpolation'. *Comput. Methods Appl. Mech. Eng.*, **19**, 59–98 (1979).
16. B. P. Leonard, 'Simple high-accuracy resolution program for convective modelling of discontinuities', *Int. j. numer. methods fluids*, **8**, 1291–1318 (1988).
17. C. Hirsch, *Numerical Computation of Internal and External Flows*, Vol. 1, Wiley, Chichester, 1988.
18. M. Bar-Lev and H. T. Yang, 'Initial flow field over an impulsively started circular cylinder', *J. Fluid Mech.*, **72**, 625–647 (1975).
19. A. Roshko, 'On the development of turbulent wake from vortex streets, *NACA Tech. Rep. 1191*. 1954.
20. N. Kondo, 'Third-order upwind element solutions of high Reynolds number flows', *Comput. Methods Appl. Mech. Eng.*, **112**, 227–251 (1994).

21. S. Goldstein (ed.), *Modern Developments in Fluid Dynamics*, Vol. 1, Dover, New York, 1965.
22. A. Fage and F. C. Johansen, 'On the flow of air behind an inclined flat plate of infinite span', *Proc. R. Soc. Lond. A*, **116**, 170–197 (1927).
23. F. M. Najjar and S. P. Vanka, 'Simulations of the unsteady separated flow past a normal flat plate'. *Int. j. numer. methods fluids*, **21**, 525–547 (1995).